Facile Synthesis of Nb_2O_5@Carbon Core–Shell Nanocrystals with Controlled Crystalline Structure for High-Power Anodes in Hybrid Supercapacitors

Eunho Lim,[†] Changshin Jo,[‡] Haegyeom Kim,[§] Mok-Hwa Kim,[∥] Yeongdong Mun,[‡] Jinyoung Chun,[‡] Youngjin Ye,[‡] Jongkook Hwang,[‡] Kyoung-Su Ha,[⊥] Kwang Chul Roh,[∥] Kisuk Kang,[§,⊹] Songhun Yoon,[*,#] and Jinwoo Lee[*,†,‡]

[†]School of Environmental Science and Engineering, Pohang University of Science and Technology (POSTECH), Pohang, Kyungbuk 790-784, Republic of Korea, [‡]Department of Chemical Engineering, Pohang University of Science and Technology (POSTECH), Pohang, Kyungbuk 790-784, Republic of Korea, [§]Department of Materials Science and Engineering, Research Institute of Advanced Materials (RIAM), Seoul National University, 599 Gwanak-Ro, Gwanak-Gu, Seoul 151-742, Republic of Korea, [⊥]Department of Chemical and Biomolecular Engineering, Sogang University, 35 Baekbeom-Ro, Mapo-Gu, Seoul 121-742, Republic of Korea, [∥]Energy and Environmental Division, Korea Institute of Ceramic Engineering and Technology (KICET), 101 Soho-Ro, Jinju, Gyeongnam 660-031, Republic of Korea, [⊹]Center for Nanoparticle Research, Institute for Basic Science (IBS), Seoul National University, Seoul 151-742, Republic of Korea, and [#]Department of Integrative Engineering, Chung-Ang University, 221, Heukseok-Dong, Dongjak-Gu, Seoul 156-756, Republic of Korea

ABSTRACT Hybrid supercapacitors (battery-supercapacitor hybrid devices, HSCs) deliver high energy within seconds (excellent rate capability) with stable cyclability. One of the key limitations in developing high-performance HSCs is imbalance in power capability between the sluggish Faradaic lithium-intercalation anode and rapid non-Faradaic capacitive cathode. To solve this problem, we synthesize Nb_2O_5@carbon core–shell nanocyrstals (Nb_2O_5@C NCs) as high-power anode materials with controlled crystalline phases (orthorhombic (*T*) and pseudohexagonal (*TT*)) *via* a facile one-pot synthesis method based on a water-in-oil microemulsion system. The synthesis of ideal *T*-Nb_2O_5 for fast Li^+ diffusion is simply achieved by controlling the microemulsion parameter (*e.g.*, pH control). The *T*-Nb_2O_5@C NCs shows a reversible specific capacity of ~180 mA h g^{-1} at 0.05 A g^{-1} (1.1–3.0 V *vs* Li/Li^+) with rapid rate capability compared to that of *TT*-Nb_2O_5@C and carbon shell-free Nb_2O_5 NCs, mainly due to synergistic effects of (i) the structural merit of *T*-Nb_2O_5 and (ii) the conductive carbon shell for high electron mobility. The highest energy (~63 W h kg^{-1}) and power (16 528 W kg^{-1} achieved at ~5 W h kg^{-1}) densities within the voltage range of 1.0–3.5 V of the HSC using *T*-Nb_2O_5@C anode and MSP-20 cathode are remarkable.

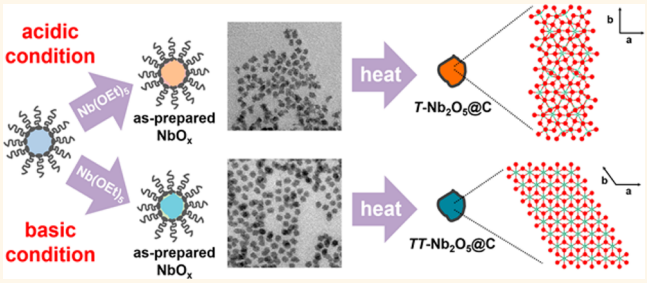

KEYWORDS: orthorhombic Nb_2O_5 nanocrystals · controlled crystal structures · core–shell nanostructures · high-power anodes · hybrid supercapacitors

With the growing market for hybrid electric vehicles (HEVs) and large-scale energy-storage systems, the worldwide interest in energy-storage systems has increased in recent years. In particular, lithium-ion batteries (LIBs) and supercapacitors (SCs) have been the subject of active research and discussion. However, there has been a clear research boundary between them because of their obviously distinct charge-storage mechanisms, although they are composed of similar components, such as electrodes, separators, and electrolytes.[1] For example, LIBs deliver high energy using intercalation-, conversion-, and alloying-mechanisms, while SCs provide high power and cycle stability through a fast physisorption of electrolyte ions at the interface between electrode and electrolyte.[2,3] Recently, this obvious boundary has, however, become vague because of the advance in nanoscience and appearance of high

* Address correspondence to yoonshun@cau.ac.kr, jinwoo03@postech.ac.kr.

Received for review April 30, 2015 and accepted June 20, 2015.

Published online June 20, 2015
10.1021/acsnano.5b02601

energy/power electrode materials. In the LIB field, the use of nanostructured (or intrinsically high-power) electrodes has resulted in improved rate capability, as well as long-term cyclability.[4−6] On the other hand, the charge-storage capacity in well-designed carbonaceous materials in SCs has been improved, thereby resulting in enhanced energy density.[7−12]

With the advancement in their respective field, the LIB−SC hybrid energy-storage systems (denoted as hybrid supercapacitors, HSCs) in aqueous and nonaqueous media have emerged and attracted much attentions in recent years.[13−17] In particular, nonaqueous HSCs deliver high energy density within seconds (fast charging/discharging) and exhibit high cycle stability. The unique features of HSCs are generally attributed to the combination of two different types of charge-storage mechanisms that are redox (Faradaic) and ion physisorption (non-Faradaic) reactions. HSCs are usually composed of high-power electrodes (*e.g.*, $Li_4Ti_5O_{12}$ and TiO_2)[18−20] of LIBs and carbonaceous electrodes[21,22] of SCs. Because of their excellent rate capability and cycle stability, carbonaceous electrodes have been widely used in the cathode part of HSCs.[23] However, the rate capability in the anode part is still unsatisfactory because of the sluggish redox reaction. Therefore, to achieve high energy/power densities in HSCs, advanced high-power anode materials are necessary to balance the electrode performances between anodes and cathodes.

To improve the kinetics and capacity in anodes, many researchers have introduced downsizing of electrode materials to the nanometer range and thereby achieved increased reversible capacity, stable cycle performance, and rapid rate capability, mainly because of the enlarged electrode−electrolyte interface area and shortened diffusion lengths for both Li^+ and electron transport.[6,24−29] Another effective approach is to introduce promising high-power anode materials. Among the possible candidates, niobium pentoxide (Nb_2O_5) is worthy of notice because of (i) its higher theoretical capacity (~200 mA h g^{-1}) than that of conventional high-power electrodes ($Li_4Ti_5O_{12}$ and TiO_2, ~170 mA h g^{-1}). This property could be helpful in improving the energy density of HSCs, calculated by using the following equation: $E = \Delta V \times C$, where C is the capacity and ΔV is the operation voltage of the HSC.[30−34] Compared with the commercial Li-ion capacitors (LICs) using graphite anode, the energy density of Nb_2O_5-based HSCs would be somewhat lower due to relatively higher lithium storage voltage and lower capacity of the Nb_2O_5 anode. However, unlike LICs, (ii) the Nb_2O_5-based HSCs working in the safe voltage range are free of the potential safety problems associated with the electrolyte decomposition, which can result in stable cycle life. In addition, (iii) the Nb_2O_5-based HSCs does not require the high-priced and inefficient prelithiation of anode materials, which is essential to achieve high energy density with stable cycle performance in the fabrication of commercial LICs.[14,35,36] Finally, (iv) its excellent rate capability derived from pseudocapacitive intercalation reactions could lead to outstanding power density of HSCs by balancing the fast kinetics of the cathode.[37]

However, to exploit the advantageous abilities of Nb_2O_5-based electrodes, there are several essential prerequisites. First, the electrochemical performance of Nb_2O_5 is highly dependent on its crystal structure and nanomorphology.[34,38] Nb_2O_5 usually possesses various crystalline phases characterized by amorphous, pseudohexagonal (*TT*) and orthorhombic (*T*) structures, depending on a variety of variables including heat-treatment conditions, precursors, impurities, synthesis methods, and so forth.[39] According to Dunn *et al.*, *T*-Nb_2O_5 designed in the form of mesostructures or nanocrystals (NCs) is more efficient for the application as high-power anode material than the other phases.[34,40] Previous studies concluded that the excellent capacity and rate performance of nanostructured *T*-Nb_2O_5 could be derived from (i) Li^+ insertion along favored crystallographic pathways[37,38] and (ii) open channels of interconnected NbO_x sheets leading to reduced energy barriers and improved local charge transfer in the structures.[41] However, development of nanostructured *T*-Nb_2O_5 has been recognized as an insurmountable obstacle because *T*-Nb_2O_5 is generally formed at high temperature (>600 °C).[42] As well-known, nanostructured materials can be easily collapsed or sintered at high temperatures.[43,44] The second problem is that Nb_2O_5 has poor electrical conductivity (~3 × 10^{-6} S cm^{-1}).[45] Hence, post-treatments (*e.g.*, carbon coating)[46] or introduction of conductive scaffolds such as carbon nanotube (CNT)[45] and carbide-derived carbon (CDC)[42] are necessary. However, such processes require additional steps like functionalization of the CNT surface or suffer from limited metal-oxide loading on the CDC.

In this work, we designed *T*-Nb_2O_5@carbon core−shell nanocrystals (*T*-Nb_2O_5@C NCs) by using a facile one-pot synthesis method based on a water-in-oil microemulsion system. In addition, for the first time, we propose a useful method for easily controlling the crystal structures (*T*- and *TT*-phases) of Nb_2O_5. To the best of our knowledge, such *T*-Nb_2O_5@C NCs have not yet been synthesized by a straightforward synthesis method. The controlled crystalline structures significantly affected the anode performance. Finally, we demonstrate the suitability of *T*-Nb_2O_5@C NCs as anode material for HSCs. The *T*-Nb_2O_5@C NCs-based HSCs possibly represent a promising energy-storage device with high energy (~63 W h kg^{-1}) and power (16 528 W kg^{-1}, achieved at ~5 W h kg^{-1}, 1 s discharge rate) densities.

RESULTS AND DISCUSSION

Figure 1 shows the synthesis procedures of the Nb_2O_5@C NCs. We prepared the water-in-oil microemulsion system with cyclohexane, surfactant (Igepal CO-520), 75 mM HCl (or HNO_3) or NaOH (or KOH) aqueous solutions, and ethanol (EtOH). It is important to note that the 75 mM aqueous solutions used as both reactant (H_2O) and acid (or base) catalyst were employed to not only induce the sol−gel reaction of niobium(V) ethoxide, but also control the reaction rate of niobium(V) ethoxide.[47] In addition, the aqueous catalyst solutions play highly important roles in the formation of the desired crystalline phase (*T*-phase) of Nb_2O_5, which will be further discussed later. For the synthesis of as-prepared NbO_x NCs, niobium(V) ethoxide was added to the prepared microemulsion system. Figure 1a and b show that the as-prepared NbO_x NCs of uniform size are well synthesized in each water-pool and wrapped by surfactants in domains of oil (reverse micelles or nanoreactors), regardless of the types of the catalyst solutions. Uncontrolled agglomeration of as-prepared NbO_x NCs can be easily prevented by surfactants on the NC surfaces and charges generated after catalytic reactions in the microemulsion system. The sizes of as-prepared NbO_x NCs synthesized using different types of aqueous catalysts are approximately 12.9 (acid catalyst, 75 mM HCl) and 12.1 (base catalyst, 75 mM NaOH) nm. In contrast, the as-prepared NbO_x NCs synthesized under the same condition with the NCs in the Figure 1a without cyclohexane are highly irregular and agglomerated as shown in Supporting Information Figure S1 because the nanosized/stable reverse micelles in the water/ethanol-based system are not well formed. Finally, the as-prepared NbO_x NCs were collected by centrifugation and then heat-treated in Ar atmosphere at 600 °C for 2 h. The heat-treatment process under inert condition (Ar flow) not only promotes the conversion of as-prepared NbO_x NCs to crystallized Nb_2O_5 NCs, such as *T*- and *TT*-Nb_2O_5, but also leads to the formation of conductive carbon shells (carbonization of the surfactant) wrapping the Nb_2O_5 NCs. Such Nb_2O_5@carbon core−shell structures were easily achieved through the facile one-pot synthesis.

It was reported by Dunn, Gogotsi *et al.* that *T*-Nb_2O_5, which is highly desirable for application as a high-power anode material than the other crystalline phases,[38] can be obtained *via* heat-treatment of as-prepared NbO_x at temperatures higher than 600 °C in an oxygen-containing atmosphere.[42] In contrast, heat-treatment in an oxygen-free atmosphere causes the formation of *TT*-Nb_2O_5 because its hexagonal unit cell includes structural defects in the form of some oxygen atoms per unit cell. This implies that some oxygen atoms are replaced by vacancies.[40,48,49] Each Nb atom is located at the center of four, five, or six oxygen atoms within the *a*−*b* plane, and Nb−O−Nb−O chains establish the connection along the *c*-axis. *T*-Nb_2O_5 has an orthorhombic unit cell in which each Nb atom is surrounded by six or seven oxygen atoms forming distorted polyhedra, such as octahedral or pentagonal bipyramids. The polyhedra are linked by edge- or corner-sharing in the *a*−*b* plane and by corner-sharing along the *c*-axis as shown in Figure 1c and d.[50,51] Such a structural feature of *T*-Nb_2O_5 with open and layered structure (Supporting Information Figure S2) allows rapid ion transport throughout the *a*−*b* plane, resulting in excellent rate

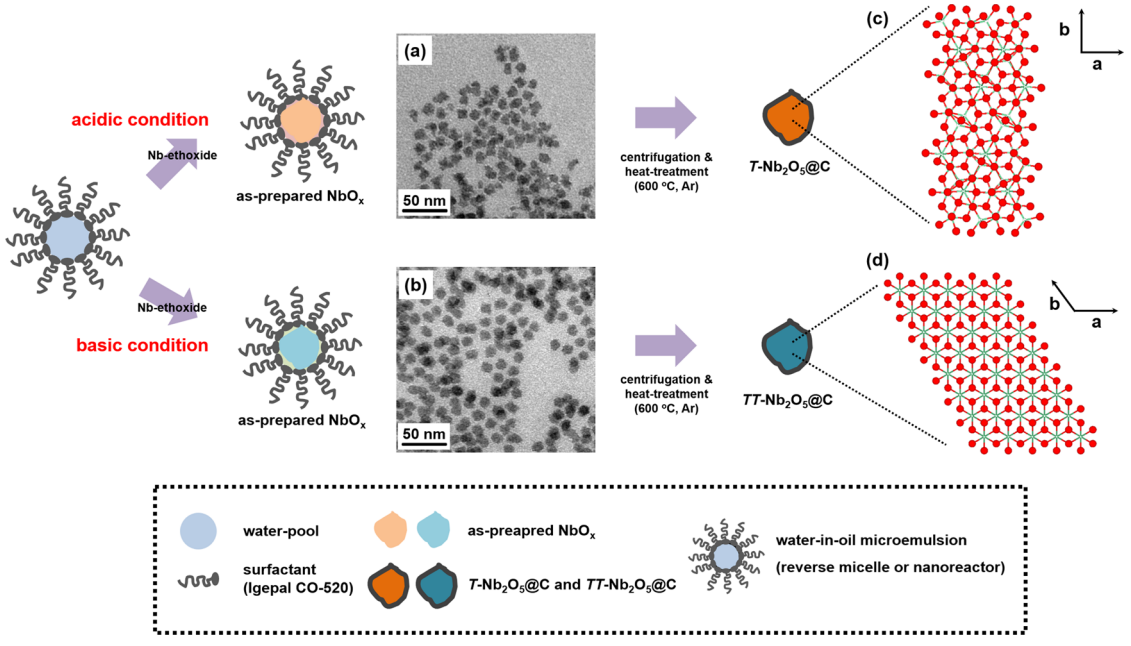

Figure 1. Schematic diagram of the synthesis procedures of Nb_2O_5@C NCs and TEM images of as-prepared NbO_x NCs synthesized using 75 mM (a) HCl and (b) NaOH aqueous catalysts. Structural schemes of (c) *T*-Nb_2O_5 and (d) *TT*-Nb_2O_5 (green ●, Nb atom; red ●, O atom).

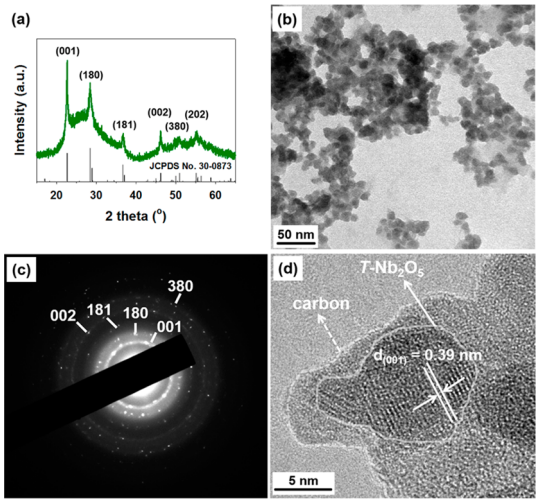

Figure 2. Characterization results of *T*-Nb_2O_5@C: (a) XRD pattern, (b) TEM image, (c) SAED pattern, and (d) HR-TEM image.

capability.[34] Thus, heat-treatment in an oxygen-containing atmosphere is essential for attaining the preferred *T*-Nb_2O_5. However, the oxygen-containing atmosphere is not suitable for synthesizing the Nb_2O_5@C core–shell structures *via* a straightforward method as it burns off the surfactants. Contrary to the expected results, even if the heat-treatment is carried out in oxygen-free atmosphere to obtain the core–shell structures, X-ray diffraction (XRD) patterns (Figure 2a) of Nb_2O_5 NCs synthesized under acidic conditions and heat-treated at 600 °C (use of 75 mM HCl or HNO_3, see Supporting Information Figure S3a and c) well match the orthorhombic phase (*T*-phase, JCPDS No. 30-0873) of Nb_2O_5. On the other hand, Nb_2O_5 NCs synthesized under basic conditions (75 mM NaOH or KOH) show a different crystal structure, namely the pseudohexagonal phase (*TT*-phase, JCPDS No. 28-0317), as shown in Supporting Information Figure S3b and d. The XRD patterns of Nb_2O_5 NCs synthesized under basic conditions never show the *T*-phase, even though the heat-treatment temperatures are sufficiently varied in the ranges of 500–900 °C (Supporting Information Figure S3b and d). In short, with increasing heat-treatment temperature, the as-prepared NbO_x NCs were converted first to amorphous Nb_2O_5 and, then, to *T*- or *TT*-Nb_2O_5 in regular succession. NbO_2 and a small amount of monoclinic Nb_2O_5 (*H*-Nb_2O_5) were also developed at approximately 800–900 °C. We reveal for the first time that the appropriate pH condition is a highly important factor for controlling the crystalline phases of Nb_2O_5. Niobium oxide sols (as-prepared NbO_x) formed by sol–gel reaction of niobium(V) ethoxide under acidic conditions might contain a sufficient amount of oxygen sources, mainly by the presence of abundant hydroxyl groups (–OH) in the sols. The acidic condition promotes the hydrolysis of metal alkoxides accompanying inhibited inorganic condensation when compared to the basic condition.[52,53] Therefore, the as-prepared NbO_x

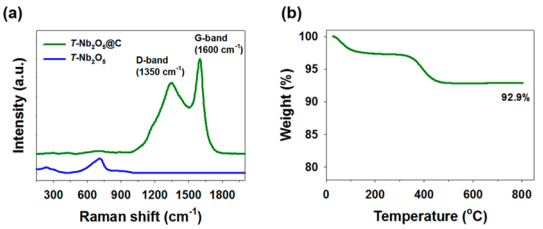

Figure 3. Characterization results of *T*-Nb_2O_5@C: (a) Raman spectra and (b) TGA profile.

obtained by acidic catalysis can be transformed to *T*-Nb_2O_5, although the heat-treatment was carried out under the oxygen-free condition. On the other hand, the crystalline phase of as-prepared NbO_x produced using basic catalysts was clearly pseudohexagonal. This is because the oxygen atoms in the unit cells can be replaced by (i) vacancies because of the inert heat-treatment condition or by (ii) impurities (*e.g.*, OH^-) derived from the basic catalysts (NaOH and KOH).[49,54] From these results, we suggest that the change in the Nb_2O_5 crystal structures arises from the chemical state of as-prepared NbO_x synthesized by the sol–gel reaction of niobium(V) ethoxide (Supporting Information Figure S4). During heat-treatment in the inert gas, the change in the Nb_2O_5 crystal structure is influenced by several experimental conditions, such as pH and heat-treatment temperatures.

The size and morphology of the *T*-Nb_2O_5@C NCs were characterized by transmission electron microscopy (TEM). Figure 2b shows that the sizes of the *T*-Nb_2O_5@C NCs are estimated to be approximately 13 nm, which is highly advantageous for application as a high-power electrode because of the shortened diffusion length.[6] After the heat-treatment at high temperature, the maintenance of nanosized crystals could be due to (i) the position of the as-prepared NbO_x NCs within independent nanoreactors (water-pools) and (ii) the conversion of surfactants to mechanically stable carbon shells. The *d*-spacings calculated from selected area electron diffraction (SAED) patterns are 0.39, 0.31, 0.24, 0.19, and 0.16 nm (Figure 2c) and well match the *d*-spacing values of the (001), (180), (181), (002), and (380) planes of *T*-Nb_2O_5, respectively, again demonstrating that the desired *T*-phase of Nb_2O_5 is well synthesized. From Supporting Information Figure S5, it can be also clearly seen that the planes of *TT*-Nb_2O_5@C obtained from SAED patterns are consistent with those of the corresponding XRD patterns (Supporting Information Figure S3b). High-resolution TEM (HR-TEM, Figure 2d) not only confirms the crystalline phase of the *T*-Nb_2O_5 with (001) spacing of 0.39 nm, but also proves the Nb_2O_5 core-carbon shell structure. Additionally, from Raman spectroscopy (Figure 3a), the presence of the carbon shell is confirmed by two bands around 1600 (graphitic carbon) and 1350 cm^{-1} (disordered carbon). The Raman spectrum of *T*-Nb_2O_5@C indirectly demonstrates the well-formed core–shell

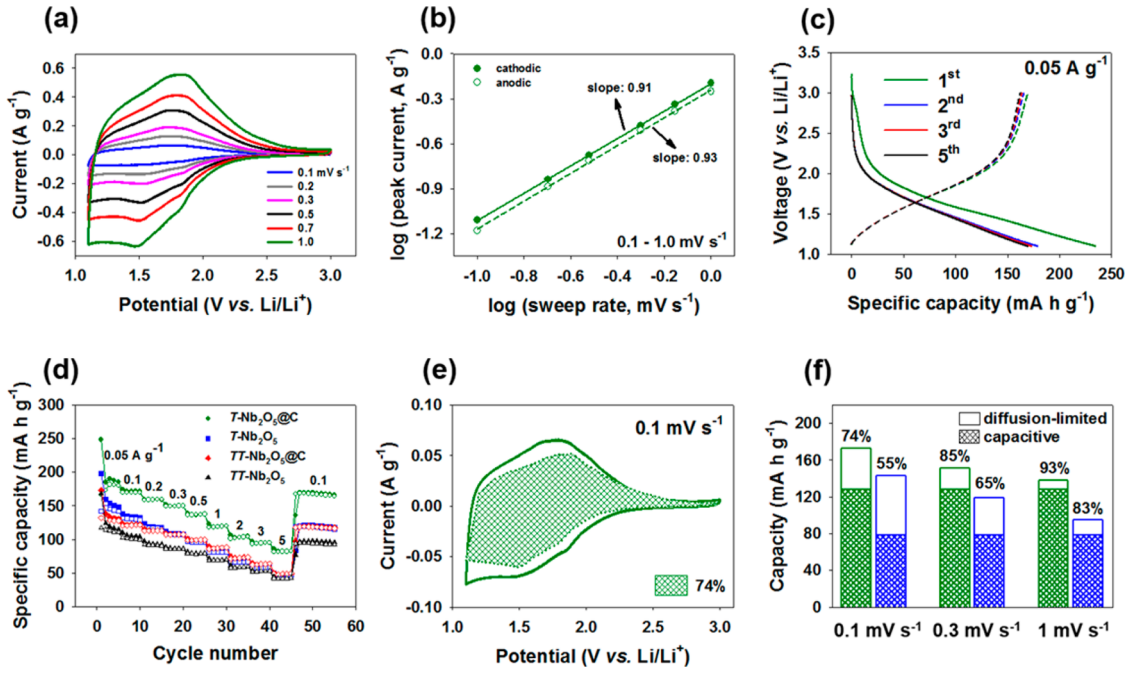

Figure 4. Electrochemical performance of Nb_2O_5/Li half-cells. (a and b) CV curves and specific peak current of *T*-Nb_2O_5@C NCs at various sweep rates from 0.1 to 1.0 mV s^{-1}. (c) Galvanostatic charge−discharge profiles of *T*-Nb_2O_5@C NCs at 0.05 A g^{-1}. (d) Comparison of the capacities in dependence of cycle number of Nb_2O_5/Li half-cells at various current densities from 0.05 to 5 A g^{-1}. (e) CV curve of *T*-Nb_2O_5@C NCs with separation between total current (solid line) and capacitive currents (shaded regions) at 0.1 mV s^{-1}. (f) Comparison of the capacities of *T*-Nb_2O_5@C (green) and *T*-Nb_2O_5 (blue) NCs at various sweep rates from 0.1 to 1.0 mV s^{-1}. (a−f) The potential range was 1.1−3.0 V (*vs* Li/Li^+).

structures, as very weak signals at 580−740 and 180−350 cm^{-1}, which are attributed to Nb−O−Nb bridging bond of distorted NbO_6 and Nb−O−Nb angular deformation, respectively, are confirmed, compared to the observed intensities of *T*-Nb_2O_5.[25,55] A thermogravimetric analysis (TGA, Figure 3b) verifies that the weight percentage of the carbon shells is ~7 wt %. The Brunauer−Emmett−Teller (BET) surface areas measured by N_2 sorption isotherms (Supporting Information Figure S6) of *T*-Nb_2O_5@C and *TT*-Nb_2O_5@C NCs were 92 and 80 m^2 g^{-1}, respectively.[56] Therefore, the Nb_2O_5@C NCs developed in this work can effectively provide shortened diffusion lengths, large electrode−electrolyte interface areas, and improved electron mobility. The experimental conditions and resulting physical parameters of Nb_2O_5@C NCs are summarized in Supporting Information Table S1 for comparison.

To show the merits of *T*-Nb_2O_5@C NCs, they were tested in half-cells using lithium metal as counter and reference electrodes before constructing the HSCs. As shown in Figure 4a, cyclic voltammetry (CV) tests at sweep rates ranging from 0.1 to 1 mV s^{-1} were performed to investigate the electrochemical behavior of the *T*-Nb_2O_5@C electrode in the potential range between 1.1 and 3.0 V (*vs* Li/Li^+). The CV exhibits broad cathodic and anodic peaks in the potential range of 1.1−2.2 V, which are similar to those of pseudocapacitive material (*e.g.,* hydrous RuO_2 in H_2SO_4), and are attributed to fast two-dimensional Li^+ transport within Nb_2O_5 crystals.[37,38] Because of the unique behavior of *T*-Nb_2O_5, the currents in the CV tests are directly proportional to the sweep rates, obeying the power law ($i = av^b$, where *a* and *b* are adjustable parameters, *i* is the current (A), and *v* is the potential sweep rate (mV s^{-1})). From the *b* values, it is feasible to distinguish between the capacitive contribution ($i = av^1$) and the diffusion-limited contribution ($i = av^{1/2}$). In Figure 4b, the *b* values of *T*-Nb_2O_5@C NCs are estimated to be nearly 1. This demonstrates that the kinetics of *T*-Nb_2O_5@C NCs is surface-controlled and quite fast and explains why *T*-Nb_2O_5 provides outstanding rate capability compared to other conventional high-power anode materials (TiO_2 and $Li_4Ti_5O_{12}$) that are based on diffusion-limited charge-storage mechanisms. From the galvanostatic charge−discharge (delithiation−lithiation) voltage profiles (Figure 4c), the continuous change of the potential upon charging/discharging well matches with the CV shapes, with reversible capacity of ~180 mA h g^{-1} at 0.05 A g^{-1} after first cycle. The first irreversible capacity loss is generally attributable to some irreversible side reactions inside the nanostructured electrode materials.[30] The excellent electrochemical properties of *T*-Nb_2O_5@C NCs are further highlighted by rate capability tests. Supporting Information Figure S7 demonstrates that the *T*-Nb_2O_5@C NCs maintain highly similar charge−discharge profiles on increasing current densities from 0.05 to 5 A g^{-1}. The *T*-Nb_2O_5@C NCs delivered much higher specific capacity with excellent rate capability

(~90 mA h g^{-1} at 5 A g^{-1}) than *TT*-Nb_2O_5@C NCs, mainly because of (i) sufficient Li^+ storage sites along ideal crystallographic pathways,[38] (ii) open and layered structure for facile Li^+ diffusion,[34] and (iii) single-phase reaction[37] and negligible changes to the lattice constants[38]/unit-cell volume[57] during Li^+ insertion/extraction. It should be mentioned that the electrochemical properties of the Nb_2O_5@C NCs are much more outstanding than those of the carbon shell-free Nb_2O_5 NCs, obviously demonstrating that the carbon shell plays a vital role in enhancing the electrochemical performance. From these electrochemical results, the development of a simple method for the controlled synthesis of the preferred crystal structure/nanomorphology and active material/carbon composite structure can be considered as a remarkable advancement in the energy-storage field.

To further obtain insight into the role of the carbon shell of *T*-Nb_2O_5@C NCs in the improved rate capability and capacity, we quantitatively separated contributions of the capacitive and diffusion-limited elements. The relationship $i = av^b$ can be divided into two terms including capacitive (k_1v) and diffusion-limited effects ($k_2v^{1/2}$), as follows:[6,58]

$$i = k_1v + k_2v^{1/2} \quad (1)$$

where i is the current (A) at a fixed potential, v is the scan rate (mV s^{-1}), and k_1 and k_2 are suitable values. By rearranging eq 1, $i/v^{1/2} = k_1v^{1/2} + k_2$ is obtained and then, k_1 and k_2 are determined by plotting $v^{1/2}$ *vs* $i/v^{1/2}$ (see Supporting Information Figure S8). The values k_1 and k_2 characterize the capacitive and diffusion-limited effects at fixed potential. As a result of this analysis, Figure 4e shows that ~74% of the total capacity of *T*-Nb_2O_5@C NCs is derived from capacitive mechanisms. Compared with the carbon shell-free *T*-Nb_2O_5 NCs, the *T*-Nb_2O_5@C NCs delivered much higher specific capacity with improved capacitive contributions at various scan rates in the range of 0.1−1.0 mV s^{-1} (Figure 4f). This clearly implies that *T*-Nb_2O_5@C NCs offer more useful pathways for electrons to Nb_2O_5 surface sites *via* the introduction of the carbon shell, resulting in enhanced capacity and rate performance.[45]

Additionally, commercial activated carbon (MSP-20) as a cathode material of the HSC was tested in half-cells, as shown in Supporting Information Figure S9. The MSP-20 cathode delivered the capacity of ~60 mA h g^{-1} with linear charge−discharge profiles in the potential range between 3.0 and 4.5 V (*vs* Li/Li^+). In the corresponding CV data (Supporting Information Figure S9c), a rectangular profile is also confirmed, implying that the MSP-20 cathode operates *via* non-Faradaic capacitive reactions.

To further verify the feasibility of *T*-Nb_2O_5@C NCs for HSC applications, we designed HCSs based on *T*-Nb_2O_5@C NCs as anode and MSP-20 as cathode. As the charge and discharge currents increase, the degree of power loss in both electrodes, in particular at high currents, could be significantly different because of the difference of their rate capabilities.[59] Thus, considering the rate capability and working voltage of each electrode in various current densities, the weight ratio of the active anode and cathode materials was carefully determined to be 1:3.5 in the potential range from 1.0 to 3.5 V (Supporting Information Figure S10). Figure 5a shows asymmetric CV profiles of the HSCs at various scan rates from 1 to 20 mV s^{-1}, stemming from the combination of fast intercalation reactions at the anode and rapid electrolyte ion transport at the cathode. In Figure 5b and c, galvanostatic charge−discharge profiles, recorded at current densities from 0.03 to 8 A g^{-1} (the current densities were based on the total mass of active material in both anode and cathode) of the HSCs also do not exhibit the typical triangular shape, in agreement with the results of the CV measurements. The energy densities calculated using the galvanostatic measurements and equation E1 (see Methods section) are shown in the inset of Figure 5d. The maximum energy density of ~63 W h kg^{-1} at 0.03 A g^{-1} was achieved with the power density of ~70 W kg^{-1} calculated using equation E2. The substantial degradation of energy densities at high current densities from 3 to 8 A g^{-1} (the inset of Figure 5d) is observed, mainly due to the voltage drop caused by various resistances in the cells. Nevertheless, at the highest power density of ~16 528 W kg^{-1}, this HSC system delivered the energy density of ~5 W h kg^{-1} at 1 s discharge rate by virtue of the excellent properties of well-designed *T*-Nb_2O_5@C NCs. Moreover, after 45 cycles at various current densities, the energy density at 1 A g^{-1} was well maintained up to 1000 cycles without significant capacity fading (Figure 5d). The Ragone plots

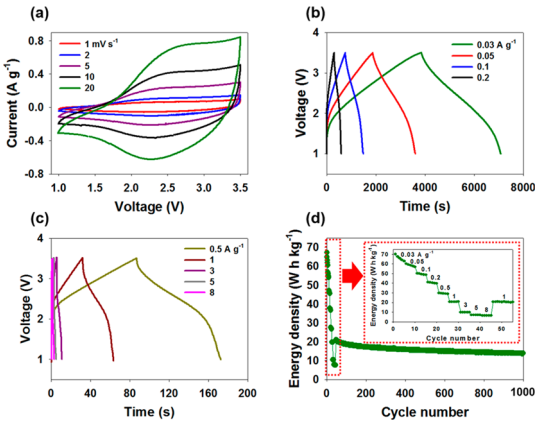

Figure 5. Electrochemical performance of the HSC using *T*-Nb_2O_5@C NCs as anode and MSP-20 as cathode material. (a) CV curves at various sweep rates from 1 to 20 mV s^{-1}. (b and c) Galvanostatic charge−discharge profiles at various current densities from 0.03 to 8 A g^{-1}. (d) Cycle stability for around 1000 cycles at the current density of 1 A g^{-1} (inset: the rate capability of the HSC was confirmed at various current densities from 0.03 to 8 A g^{-1} before cycling). (a−d) The potential range was 1.0−3.5 V.

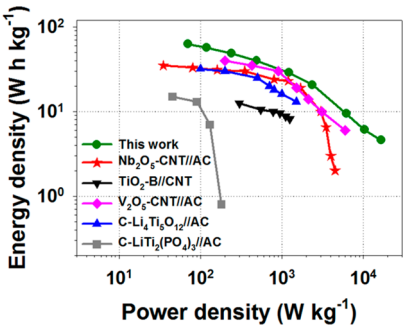

Figure 6. Ragone plots in comparison with results of other reports. HSCs based on *T*-Nb_2O_5@C//MSP-20 (green ●) are compared with HSCs using Nb_2O_5−CNT//AC (red ★),[45] TiO_2−B//CNT (black ▼),[18] V_2O_5−CNT//AC (pink ◆),[60] C−$Li_4Ti_5O_{12}$//AC (blue ▲),[19] and C-$LiTi_2(PO_4)_3$//AC (gray ■).[61]

(Figure 6) demonstrate the superior HSCs using *T*-Nb_2O_5@C NCs compared to similar HSC systems using Nb_2O_5−CNT, C−$Li_4Ti_5O_{12}$, and TiO_2−B, and *etc.*[18,19,45,60,61] In addition, it is clear from Supporting Information Figure S11 that the *T*-Nb_2O_5@C NCs-based HSC simultaneously delivering high energy and power densities could be regarded as one of the next-generation energy-storage devices. The merits of *T*-Nb_2O_5@C NCs as anode material of HSCs are as follows: (i) Shortened diffusion lengths as a consequence of well-defined nanosized Nb_2O_5, resulting in rapid charge transport (excellent rate capability). (ii) Improved charge-storage sites (superior capacity) and enhanced reactivity between electrode and electrolyte, mainly due to the controlled crystalline structure and huge surface areas of Nb_2O_5 NCs. In addition, (iii) useful pathways for electron mobility were supplied owing to formation of the carbon shell from the one-pot synthesis method. Finally, (iv) the additional carbon coating processes or use of conductive scaffolds were not required, which is beneficial from an economic standpoint.

CONCLUSIONS

In summary, we have not only developed a facile one-pot synthesis method for Nb_2O_5@carbon core−shell nanostructures, but also revealed the importance of the experimental variables to control the crystal structure of Nb_2O_5. Particularly, the appropriate pH condition was one of the most important factors for controlling the Nb_2O_5 crystalline phases in the water-in-oil microemulsion system. As a proof of the concept, *T*-Nb_2O_5@C NCs were used as anode in HSCs. The *T*-Nb_2O_5@C anode exhibited the reversible capacity of ~180 mA h g^{-1} at 0.05 A g^{-1} and excellent rate performance (~90 mA h g^{-1} at 5 A g^{-1}) within the potential range from 1.1 to 3.0 V (*vs* Li/Li^+). In addition, the *T*-Nb_2O_5@C NCs//MSP-20-based HSC system was prepared and showed outstanding electrochemical performance (maximum energy and power densities of ~63 W h kg^{-1} and ~16 528 W kg^{-1}, respectively) with high cycle stability in the voltage window of 1.0−3.5 V.

METHODS

Synthesis of the Nb_2O_5@Carbon Core−Shell Nanocrystals and Control Groups. For the synthesis of the *T*-Nb_2O_5@C NCs, microemulsion was prepared as follows. The oil phase composed of 11.5 g of Igepal CO-520 and 225 mL of cyclohexane was mixed with 1.25 mL of 75 mM HCl (or HNO_3) aqueous solution and 3 mL of ethanol. Then, 0.375 mL of niobium(V) ethoxide (1.5 mmol) was injected into the microemulsion under appropriate stirring at room temperature. After 20 min, the synthesized nanoparticles were isolated by centrifugation using a mixed solution of 1:1 (v/v) ether/*n*-hexane several times. Subsequently, the material collected from the centrifugation step was dried at 100 °C overnight. Finally, the resulting material was heat-treated in Ar atmosphere at 600 °C for 2 h. To obtain carbon shell-free *T*-Nb_2O_5, the carbon shell of *T*-Nb_2O_5@C was removed by calcination in O_2 at 450 °C for 2 h. The *TT*-Nb_2O_5@C and *TT*-Nb_2O_5 was synthesized under identical conditions as mentioned above. However, a 75 mM NaOH (or KOH) aqueous solution was used instead of 75 mM HCl (or HNO_3) aqueous solution. For synthesis of the as-prepared NbO_x shown in Supporting Information Figure S1, 11.5 g of Igepal CO-520 was mixed with 68.75 mL of 75 mM HCl aqueous solution and 160.5 mL of ethanol. And then, 0.375 mL of niobium(V) ethoxide was injected into the solution with appropriate stirring.

Physical Characterization. The crystal structure of the samples was confirmed by X-ray diffraction (XRD, Bruker D8 Advance, Cu Kα radiation). The size and morphology of the samples were characterized by transmission electron microscopy (TEM, JEM-1011, JEOL LTD) and high-resolution transmission electron microscopy (HR-TEM, JEOL JEM-2010). The carbon content in the samples was analyzed by thermogravimetric analysis (TGA, NETZSCH STA 449C thermobalance) and Raman spectroscopy (Horiba Jobin Yvon, LabRam Aramis). The BET surface areas were estimated by using a Tristar II 3020 instrument (Micromeritics Instrument Corporation).

Electrochemical Characterization. The Nb_2O_5-based electrodes for half-cell and full-cell tests were prepared by homogeneously mixing the active materials (80 wt %) with super-P carbon (10 wt %) and polyvinylidene fluoride (PVDF) (10 wt %) in *N*-methyl-2-pyrrolidone (NMP). Then, the resulting slurries were coated onto a piece of Cu foil. The electrodes were dried at 60 °C for 6 h and subsequently 110 °C for 12 h in a vacuum oven. Additionally, the dried electrodes were roll-pressed. The half-cell tests were carried out using 2032-type coin cells with Li metal as both counter and reference electrodes and 1.0 M $LiPF_6$ in ethylene carbonate/dimethyl carbonate (EC/DMC, 1:1 volume ratio, Panaxetec Co., Korea) as electrolyte. The coin cells were assembled in an Ar-filled glovebox. In addition, the mass loading of the electrodes was carefully controlled within the range of 0.9−1.1 mg cm^{-2}. The activated carbon electrodes were prepared by mixing the activated carbon (MSP-20, 90 wt %) with conductive carbon (5 wt %) and polytetrafluoroethylene (PTFE, 5 wt %). The activated carbon cells were assembled by the same as method mentioned above. For full-cell tests of the HSCs, the Nb_2O_5 electrodes used as anodes were assembled with activated carbon (MSP-20) as cathodes. The weight ratio of the anode and cathode active material was varied from 1:2.5 to 1:4.5 in the voltage range of 1.0−3.5 V to optimize the electrochemical performance. All electrochemical tests were conducted using the WBCS-3000 battery cycler (WonA Tech, Korea). The energy and power densities were calculated by numerically integrating the galvanostatic discharge curves using the equations below:[62]

$$E = \int_{t_1}^{t_2} IV\,dt \qquad \text{(E1)}$$

where I is the constant current density (A g^{-1}), V (V) is the voltage, and t_1 and t_2 are the start/end-of-discharge time (s) of HSCs, respectively, and

$$P = \frac{E}{t} \quad \text{(E2)}$$

where t is the discharge time (s).

Conflict of Interest: The authors declare no competing financial interest.

Supporting Information Available: The further characterization and electrochemical data of Nb_2O_5 samples. The Supporting Information is available free of charge on the ACS Publications website at DOI: 10.1021/acsnano.5b02601.

Acknowledgment. This research was supported by Basic Science Research Program through the National Research Foundation (NRF) funded by the Ministry of Science, ICT and Future Planning (NRF-2013R1A1A2074550). We appreciate Prof. Taeghwan Hyeon and Dr. Myoung Hwan Oh for kind comments. This article is dedicated to Prof. In-Sik Nam on the occasion of his retirement from Pohang University of Science and Technology (POSTECH)

REFERENCES AND NOTES

1. Simon, P.; Gogotsi, Y.; Dunn, B. Where Do Batteries End and Supercapacitors Begin? *Science* **2014**, *343*, 1210–1211.
2. Kang, K.; Meng, Y. S.; Breger, J.; Grey, C. P.; Ceder, G. Electrodes with High Power and High Capacity for Rechargeable Lithium Batteries. *Science* **2006**, *311*, 977–980.
3. Yuan, F.-W.; Yang, H.-J.; Tuan, H.-Y. Alkanethiol-Passivated Ge Nanowires as High-Performance Anode Materials for Lithium-Ion Batteries: The Role of Chemical Surface Functionalization. *ACS Nano* **2012**, *6*, 9932–9942.
4. Pol, V. G.; Kang, S.-H.; Calderon-Moreno, J. M.; Johnson, C. S.; Thackeray, M. M. Autogenic Reactions for Preparing Carbon-Encapsulated, Nanoparticulate TiO_2 Electrodes for Lithium-Ion Batteries. *J. Power Sources* **2010**, *195*, 5039–5043.
5. Poizot, P.; Laruelle, S.; Grugeon, S.; Dupont, L.; Tarascon, J. M. Nano-Sized Transition-Metal Oxides as Negative-Electrode Materials for Lithium-Ion Batteries. *Nature* **2000**, *407*, 496–499.
6. Wang, J.; Polleux, J.; Lim, J.; Dunn, B. Pseudocapacitive Contributions to Electrochemical Energy Storage in TiO_2 (Anatase) Nanoparticles. *J. Phys. Chem. C* **2007**, *111*, 14925–14931.
7. Chmiola, J.; Largeot, C.; Taberna, P.-L.; Simon, P.; Gogotsi, Y. Monolithic Carbide-Derived Carbon Films for Micro-Supercapacitors. *Science* **2010**, *328*, 480–483.
8. Pech, D.; Brunet, M.; Durou, H.; Huang, P.; Mochalin, V.; Gogotsi, Y.; Taberna, P.-L.; Simon, P. Ultrahigh-Power Micrometer-Sized Supercapacitors Based on Onion-Like Carbon. *Nat. Nanotechnol.* **2010**, *5*, 651–654.
9. Yoon, S.; Lee, J.; Hyeon, T.; Oh, S. M. Electric Double-Layer Capacitor Performance of a New Mesoporous Carbon. *J. Electrochem. Soc.* **2000**, *147*, 2507–2512.
10. Liu, J.; Zhang, L.; Wu, H. B.; Lin, J.; Shen, Z.; Lou, X. W. D. High-Performance Flexible Asymmetric Supercapacitors Based on a New Graphene Foam/Carbon Nanotube Hybrid Film. *Energy Environ. Sci.* **2014**, *7*, 3709–3719.
11. Mun, Y.; Jo, C.; Hyeon, T.; Lee, J.; Ha, K.-S.; Jun, K.-W.; Lee, S.-H.; Hong, S.-W.; Lee, H. I.; Yoon, S. Simple Synthesis of Hierarchically Structured Partially Graphitized Carbon by Emulsion/Block-Copolymer Co-Template Method for High Power Supercapacitors. *Carbon* **2013**, *64*, 391–402.
12. Jo, C.; An, S.; Kim, Y.; Shim, J.; Yoon, S.; Lee, J. Nano-Graphite Functionalized Mesocellular Carbon Foam with Enhanced Intra-Penetrating Electrical Percolation Networks for High Performance Electrochemical Energy Storage Electrode Materials. *Phys. Chem. Chem. Phys.* **2012**, *14*, 5695–5704.
13. Naoi, K.; Naoi, W.; Aoyagi, S.; Miyamoto, J.-i.; Kamino, T. New Generation "Nanohybrid Supercapacitor". *Acc. Chem. Res.* **2012**, *46*, 1075–1083.
14. Naoi, K.; Ishimoto, S.; Miyamoto, J.-i.; Naoi, W. Second Generation 'Nanohybrid Supercapacitor': Evolution of Capacitive Energy Storage Devices. *Energy Environ. Sci.* **2012**, *5*, 9363–9373.
15. Lee, J. H.; Shin, W. H.; Lim, S. Y.; Kim, B. G.; Choi, J. W. Modified Graphite and Graphene Electrodes for High-Performance Lithium Ion Hybrid Capacitors. *Mater. Renew. Sustain. Energy* **2014**, *3*, 1–8.
16. Shen, L.; Yu, L.; Wu, H. B.; Yu, X.-Y.; Zhang, X.; Lou, X. W. Formation of Nickel Cobalt Sulfide Ball-in-Ball Hollow Spheres with Enhanced Electrochemical Pseudocapacitive Properties. *Nat. Commun.* **2015**, *6*, 6694–6701.
17. Peng, S.; Li, L.; Wu, H. B.; Madhavi, S.; Lou, X. W. D. Controlled Growth of $NiMoO_4$ Nanosheet and Nanorod Arrays on Various Conductive Substrates as Advanced Electrodes for Asymmetric Supercapacitors. *Adv. Energy Mater.* **2014**, *5*, 1401172.
18. Wang, Q.; Wen, Z.; Li, J. A Hybrid Supercapacitor Fabricated with a Carbon Nanotube Cathode and a TiO_2−B Nanowire Anode. *Adv. Funct. Mater.* **2006**, *16*, 2141–2146.
19. Jung, H.-G.; Venugopal, N.; Scrosati, B.; Sun, Y.-K. A High Energy and Power Density Hybrid Supercapacitor Based on an Advanced Carbon-Coated $Li_4Ti_5O_{12}$ Electrode. *J. Power Sources* **2013**, *221*, 266–271.
20. Kim, H.; Cho, M. Y.; Kim, M. H.; Park, K. Y.; Gwon, H.; Lee, Y.; Roh, K. C.; Kang, K. A Novel High-Energy Hybrid Supercapacitor with an Anatase TiO_2−Reduced Graphene Oxide Anode and an Activated Carbon Cathode. *Adv. Energy Mater.* **2013**, *3*, 1500–1506.
21. Kim, H.; Park, K. Y.; Cho, M. Y.; Kim, M. H.; Hong, J.; Jung, S. K.; Roh, K. C.; Kang, K. High-Performance Hybrid Supercapacitor Based on Graphene-Wrapped $Li_4Ti_5O_{12}$ and Activated Carbon. *ChemElectroChem.* **2014**, *1*, 125–130.
22. Wang, Y.; Hong, Z.; Wei, M.; Xia, Y. Layered $H_2Ti_6O_{13}$-Nanowires: A New Promising Pseudocapacitive Material in Non-Aqueous Electrolyte. *Adv. Funct. Mater.* **2012**, *22*, 5185–5193.
23. Aravindan, V.; Sundaramurthy, J.; Jain, A.; Kumar, P. S.; Ling, W. C.; Ramakrishna, S.; Srinivasan, M. P.; Madhavi, S. Unveiling $TiNb_2O_7$ as an Insertion Anode for Lithium Ion Capacitors with High Energy and Power Density. *ChemSusChem* **2014**, *7*, 1858–1863.
24. Yi, R.; Chen, S.; Song, J.; Gordin, M. L.; Manivannan, A.; Wang, D. High-Performance Hybrid Supercapacitor Enabled by a High-Rate Si-Based Anode. *Adv. Funct. Mater.* **2014**, *24*, 7433–7439.
25. Lim, E.; Kim, H.; Jo, C.; Chun, J.; Ku, K.; Kim, S.; Lee, H. I.; Nam, I.-S.; Yoon, S.; Kang, K. Advanced Hybrid Supercapacitor Based on a Mesoporous Niobium Pentoxide/Carbon as High-Performance Anode. *ACS Nano* **2014**, *8*, 8968–8978.
26. Brezesinski, T.; Wang, J.; Polleux, J.; Dunn, B.; Tolbert, S. H. Templated Nanocrystal-based Porous TiO_2 Films for Next-Generation Electrochemical Capacitors. *J. Am. Chem. Soc.* **2009**, *131*, 1802–1809.
27. Lee, S. H.; Yu, S.-H.; Lee, J. E.; Jin, A.; Lee, D. J.; Lee, N.; Jo, H.; Shin, K.; Ahn, T.-Y.; Kim, Y.-W. Self-Assembled Fe_3O_4 Nanoparticle Clusters as High-Performance Anodes for Lithium Ion Batteries *via* Geometric Confinement. *Nano Lett.* **2013**, *13*, 4249–4256.
28. Oh, M. H.; Yu, T.; Yu, S.-H.; Lim, B.; Ko, K.-T.; Willinger, M.-G.; Seo, D.-H.; Kim, B. H.; Cho, M. G.; Park, J.-H. Galvanic Replacement Reactions in Metal Oxide Nanocrystals. *Science* **2013**, *340*, 964–968.
29. Ha, D.-H.; Islam, M. A.; Robinson, R. D. Binder-Free and Carbon-Free Nanoparticle Batteries: A Method for Nanoparticle Electrodes without Polymeric Binders or Carbon Black. *Nano Lett.* **2012**, *12*, 5122–5130.
30. Kim, G.; Jo, C.; Kim, W.; Chun, J.; Yoon, S.; Lee, J.; Choi, W. TiO_2 Nanodisks Designed for Li-Ion Batteries: A Novel Strategy for Obtaining an Ultrathin and High Surface Area Anode Material at the Ice Interface. *Energy Environ. Sci.* **2013**, *6*, 2932–2938.
31. Yu, L.; Wu, H. B.; Lou, X. W. D. Mesoporous $Li_4Ti_5O_{12}$ Hollow Spheres with Enhanced Lithium Storage Capability. *Adv. Mater.* **2013**, *25*, 2296–2300.

32. Kang, E.; Jung, Y. S.; Kim, G. H.; Chun, J.; Wiesner, U.; Dillon, A. C.; Kim, J. K.; Lee, J. Highly Improved Rate Capability for a Lithium-Ion Battery Nano-$Li_4Ti_5O_{12}$ Negative Electrode *via* Carbon-Coated Mesoporous Uniform Pores with a Simple Self-Assembly Method. *Adv. Funct. Mater.* **2011**, *21*, 4349–4357.
33. Lee, J.; Jung, Y. S.; Warren, S. C.; Kamperman, M.; Oh, S. M.; DiSalvo, F. J.; Wiesner, U. Direct Access to Mesoporous Crystalline TiO_2/Carbon Composites with Large and Uniform Pores for Use as Anode Materials in Lithium Ion Batteries. *Macromol. Chem. Phys.* **2011**, *212*, 383–390.
34. Augustyn, V.; Come, J.; Lowe, M. A.; Kim, J. W.; Taberna, P.-L.; Tolbert, S. H.; Abruña, H. D.; Simon, P.; Dunn, B. High-Rate Electrochemical Energy Storage through Li^+ Intercalation Pseudocapacitance. *Nat. Mater.* **2013**, *12*, 518–522.
35. Decaux, C.; Lota, G.; Raymundo-Piñero, E.; Frackowiak, E.; Béguin, F. Electrochemical Performance of a Hybrid Lithium-Ion Capacitor with a Graphite Anode Preloaded from Lithium Bis(trifluoromethane)sulfonimide-Based Electrolyte. *Electrochim. Acta* **2012**, *86*, 282–286.
36. Park, M. S.; Lim, Y. G.; Hwang, S. M.; Kim, J. H.; Kim, J. S.; Dou, S. X.; Cho, J.; Kim, Y. J. Scalable Integration of Li_5FeO_4 towards Robust, High-Performance Lithium-Ion Hybrid Capacitors. *ChemSusChem* **2014**, *7*, 3138–3144.
37. Come, J.; Augustyn, V.; Kim, J. W.; Rozier, P.; Taberna, P.-L.; Gogotsi, P.; Long, J. W.; Dunn, B.; Simon, P. Electrochemical Kinetics of Nanostructured Nb_2O_5 Electrodes. *J. Electrochem. Soc.* **2014**, *161*, A718–A725.
38. Kim, J. W.; Augustyn, V.; Dunn, B. The Effect of Crystallinity on the Rapid Pseudocapacitive Response of Nb_2O_5. *Adv. Energy Mater.* **2012**, *2*, 141–148.
39. Kobayashi, Y.; Hata, H.; Salama, M.; Mallouk, T. E. Scrolled Sheet Precursor Route to Niobium and Tantalum Oxide Nanotubes. *Nano Lett.* **2007**, *7*, 2142–2145.
40. Kodama, R.; Terada, Y.; Nakai, I.; Komaba, S.; Kumagai, N. Electrochemical and *in situ* XAFS-XRD Investigation of Nb_2O_5 for Rechargeable Lithium Batteries. *J. Electrochem. Soc.* **2006**, *153*, A583–A588.
41. Lubimtsev, A. A.; Kent, P. R.; Sumpter, B. G.; Ganesh, P. Understanding the Origin of High-Rate Intercalation Pseudocapacitance in Nb_2O_5 Crystals. *J. Mater. Chem. A* **2013**, *1*, 14951–14956.
42. Zhang, C. J.; Maloney, R.; Lukatskaya, M. R.; Beidaghi, M.; Dyatkin, B.; Perre, E.; Long, D.; Qiao, W.; Dunn, B.; Gogotsi, Y. Synthesis and Electrochemical Properties of Niobium Pentoxide Deposited on Layered Carbide-Derived Carbon. *J. Power Sources* **2015**, *274*, 121–129.
43. Zeng, P.; Zajac, S.; Clapp, P.; Rifkin, J. Nanoparticle Sintering Simulations. *Mater. Sci. Eng., A* **1998**, *252*, 301–306.
44. Lee, J.; Orilall, M. C.; Warren, S. C.; Kamperman, M.; DiSalvo, F. J.; Wiesner, U. Direct Access to Thermally Stable and Highly Crystalline Mesoporous Transition-Metal Oxides with Uniform Pores. *Nat. Mater.* **2008**, *7*, 222–228.
45. Wang, X.; Li, G.; Chen, Z.; Augustyn, V.; Ma, X.; Wang, G.; Dunn, B.; Lu, Y. High-Performance Supercapacitors Based on Nanocomposites of Nb_2O_5 Nanocrystals and Carbon Nanotubes. *Adv. Energy Mater.* **2011**, *1*, 1089–1093.
46. Wang, X.; Yan, C.; Yan, J.; Sumboja, A.; Lee, P. S. Orthorhombic Niobium Oxide Nanowires for Next Generation Hybrid Supercapacitor Device. *Nano Energy* **2015**, *11*, 765–772.
47. Oh, M. H.; Lee, N.; Kim, H.; Park, S. P.; Piao, Y.; Lee, J.; Jun, S. W.; Moon, W. K.; Choi, S. H.; Hyeon, T. Large-Scale Synthesis of Bioinert Tantalum Oxide Nanoparticles for X-ray Computed Tomography Imaging and Bimodal Image-Guided Sentinel Lymph Node Mapping. *J. Am. Chem. Soc.* **2011**, *133*, 5508–5515.
48. Ikeya, T.; Senna, M. Change in the Structure of Niobium Pentoxide due to Mechanical and Thermal Treatments. *J. Non. Cryst. Solids* **1988**, *105*, 243–250.
49. Ko, E.; Weissman, J. Structures of Niobium Pentoxide and Their Implications on Chemical Behavior. *Catal. Today* **1990**, *8*, 27–36.
50. Rani, R. A.; Zoolfakar, A. S.; O'Mullane, A. P.; Austin, M. W.; Kalantar-Zadeh, K. Thin Films and Nanostructures of Niobium Pentoxide: Fundamental Properties, Synthesis Methods and Applications. *J. Mater. Chem. A* **2014**, *2*, 15683–15703.
51. Zhao, Y.; Zhou, X.; Ye, L.; Tsang, S. C. E. Nanostructured Nb_2O_5 Catalysts. *Nano Rev.* **2012**, *3*, 1–11.
52. Soler-Illia, G. J. d. A.; Sanchez, C.; Lebeau, B.; Patarin, J. Chemical Strategies to Design Textured Materials: From Microporous and Mesoporous Oxides to Nanonetworks and Hierarchical Structures. *Chem. Rev.* **2002**, *102*, 4093–4138.
53. Brinker, C. J.; Scherer, G. W. *Sol-Gel Science: The Physics and Chemistry of Sol-Gel Processing*; Academic Press: Boston, MA, 1990.
54. Aegerter, M. A. Sol−Gel Niobium Pentoxide: A Promising Material for Electrochromic Coatings, Batteries, Nanocrystalline Solar Cells and Catalysis. *Sol. Energy Mater. Sol. Cells* **2001**, *68*, 401–422.
55. Borgel, V.; Gershinsky, G.; Hu, T.; Theivanayagam, M. G.; Aurbach, D. $LiMn_{0.8}Fe_{0.2}PO_4/Li_4Ti_5O_{12}$, a Possible Li-Ion Battery System for Load-Leveling Application. *J. Electrochem. Soc.* **2013**, *160*, A650–A657.
56. Barrett, E. P.; Joyner, L. G.; Halenda, P. P. The Determination of Pore Volume and Area Distributions in Porous Substances. I. Computations from Nitrogen Isotherms. *J. Am. Chem. Soc.* **1951**, *73*, 373–380.
57. Kumagai, N.; Koishikawa, Y.; Komaba, S.; Koshiba, N. Thermodynamics and Kinetics of Lithium Intercalation into Nb_2O_5 Electrodes for a 2 V Rechargeable Lithium Battery. *J. Electrochem. Soc.* **1999**, *146*, 3203–3210.
58. Kim, H.; Hong, J.; Park, Y. U.; Kim, J.; Hwang, I.; Kang, K. Energy Storage: Sodium Storage Behavior in Natural Graphite Using Ether-based Electrolyte Systems. *Adv. Funct. Mater.* **2015**, *25*, 652–652.
59. Dsoke, S.; Fuchs, B.; Gucciardi, E.; Wohlfahrt-Mehrens, M. The Importance of the Electrode Mass Ratio in a Li-Ion Capacitor Based on Activated Carbon and $Li_4Ti_5O_{12}$. *J. Power Sources* **2015**, *282*, 385–393.
60. Chen, Z.; Augustyn, V.; Wen, J.; Zhang, Y.; Shen, M.; Dunn, B.; Lu, Y. High-Performance Supercapacitors Based on Intertwined CNT/V_2O_5 Nanowire Nanocomposites. *Adv. Mater.* **2011**, *23*, 791–795.
61. Aravindan, V.; Chuiling, W.; Reddy, M.; Rao, G. S.; Chowdari, B. V.; Madhavi, S. Carbon Coated Nano-$LiTi_2(PO_4)_3$ Electrodes for Non-Aqueous Hybrid Supercapacitors. *Phys. Chem. Chem. Phys.* **2012**, *14*, 5808–5814.
62. Zhang, F.; Zhang, T.; Yang, X.; Zhang, L.; Leng, K.; Huang, Y.; Chen, Y. A High-Performance Supercapacitor-Battery Hybrid Energy Storage Device Based on Graphene-Enhanced Electrode Materials with Ultrahigh Energy Density. *Energy Environ. Sci.* **2013**, *6*, 1623–1632.